Supporting Information:

Sintering pressure as a "scalpel" to enhance the thermoelectric performance of MgAgSb

Yuntiao Liao[a,1], Jun-Liang Chen[b,1], Chengyan Liu[c,*], Jisheng Liang[a], Qi Zhou[a], Ping Wang[a], Lei Miao[a,c,d,*]

[a] School of Physical Science and Technology, Guangxi University, Nanning 530004, China

[b] School of Chemistry and Chemical Engineering, Guangxi University, Nanning 530004, China

[c] Engineering Research Center of Electronic Information Materials and Devices, Ministry of Education, Guangxi Key Laboratory of Information Material, Guilin University of Electronic Technology, Guilin 541004, China

[d] Department of Materials Science and Engineering, SIT Research Laboratories, Innovative Global Program, Faculty of Engineering, Shibaura Institute of Technology, Tokyo,135-8548, Japan

* Corresponding author.

E-mail addresses: lead contact: miaolei@guet.edu.cn (L. Miao); chengyanliu@guet.edu.cn (C. Liu).

[1]These authors contributed equally.

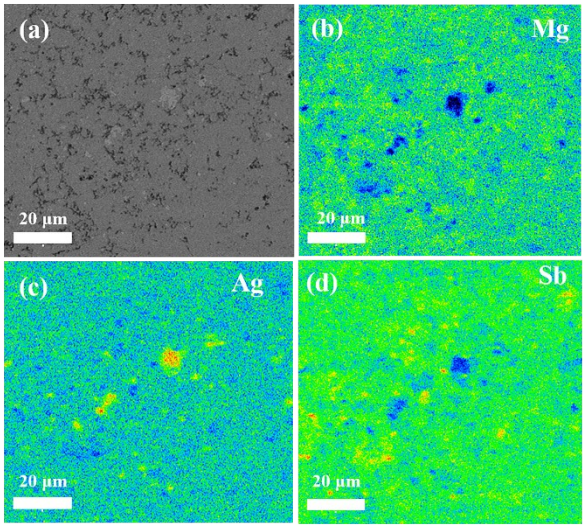

Figure S1. EPMA characterization of $MgAg_{0.95}Sb_{0.99}$ samples. (a) A back scattering electron (BSE) image; (b−d) element mapping images of Mg, Ag, and Sb of the $MgAg_{0.95}Sb_{0.99}$ sample sintered under the compressive pressure of 50 MPa.

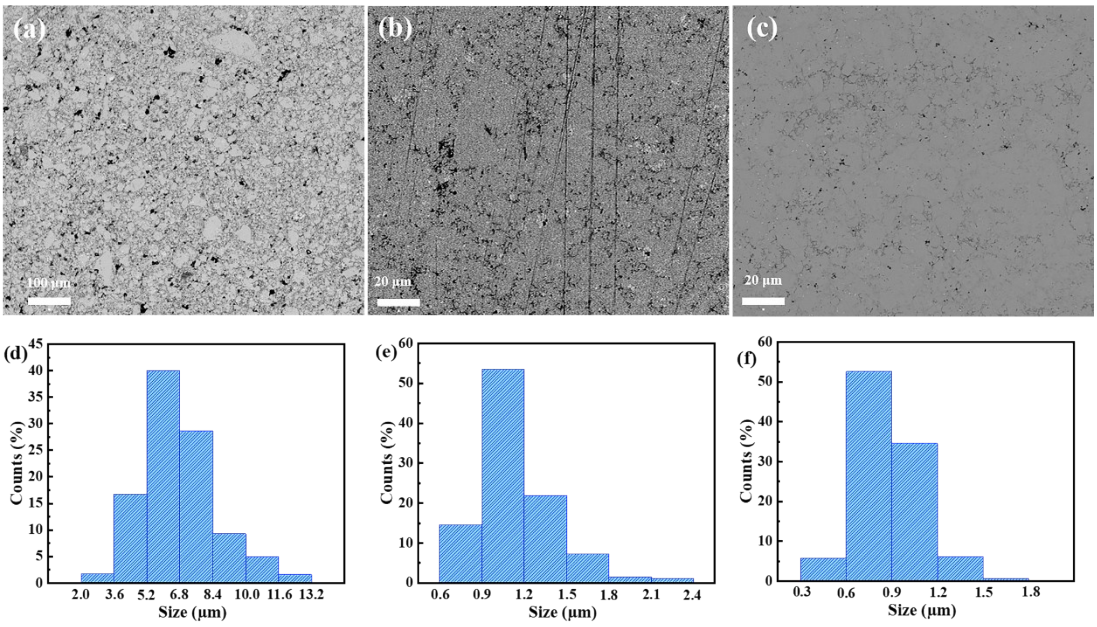

Figure S2. The back scattering electron image of $MgAg_{0.95}Sb_{0.99}$ samples sintered under the compressive pressure for (a) 20 MPa, (b) 50 MPa, and (c) 80 MPa, respectively. The statistical results of pore size for $MgAg_{0.95}Sb_{0.99}$ samples sintered under the compressive pressure for (d) 20 MPa, (e) 50 MPa, and (f) 80 MPa, respectively.

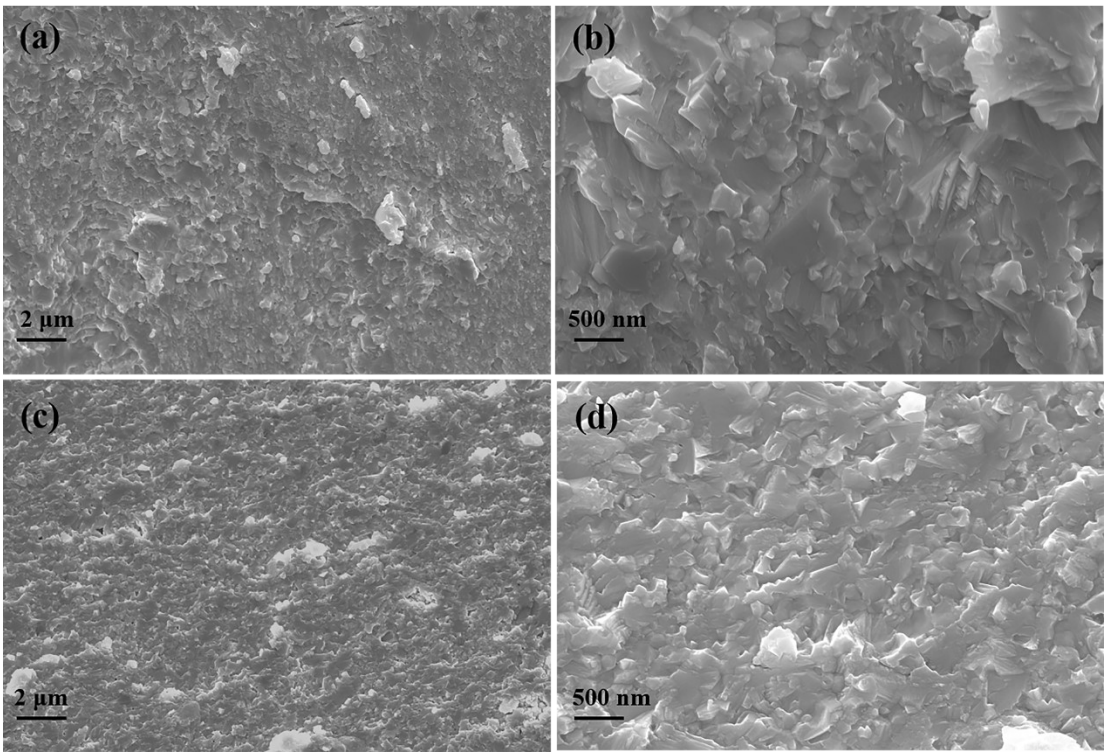

Figure S3. The SEM images of freshly fractured surface for MgAg0.95Sb0.99 samples sintered under the axial compressive stress for (a) − (b) 80MPa, and (c) − (d) 100MPa, respectively.

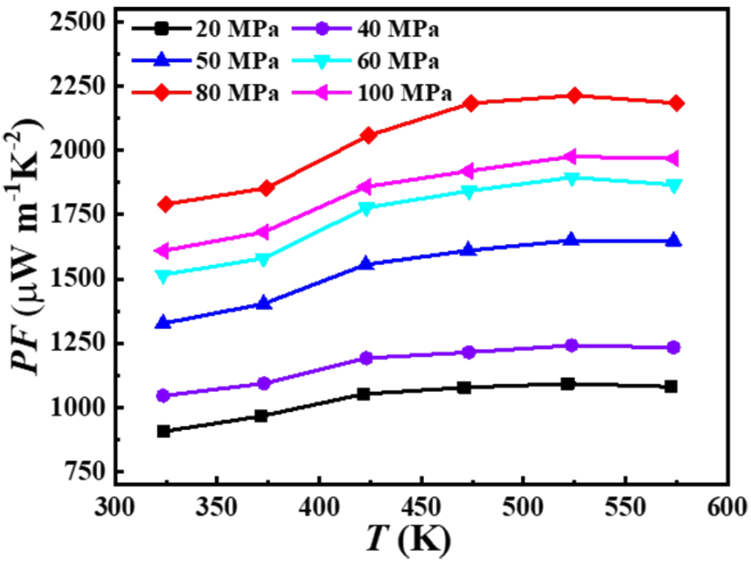

Figure S4. Temperature dependences of power factor of $MgAg_{0.95}Sb_{0.99}$ samples sintered under the compressive pressure of 20 MPa, 40 MPa, 50 MPa, 60 MPa, 80 MPa and 100 MPa, respectively.

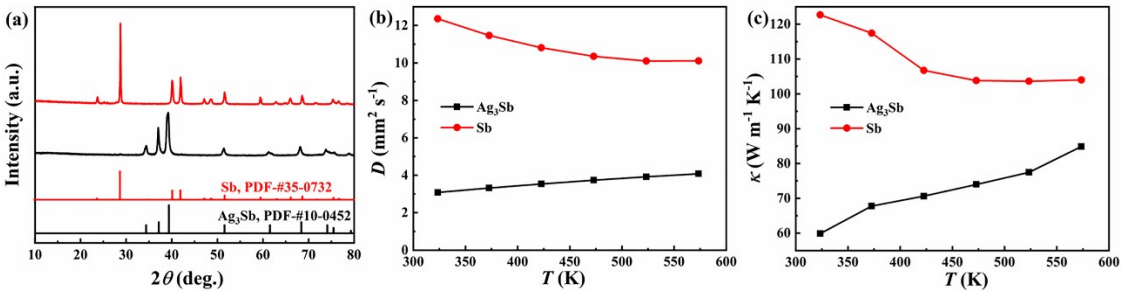

Figure S5. (a) XRD patterns of Sb and Ag_3Sb. Temperature dependence of (b) diffusivity coefficient and (c) thermal conductivity for Sb and Ag_3Sb, respectively.

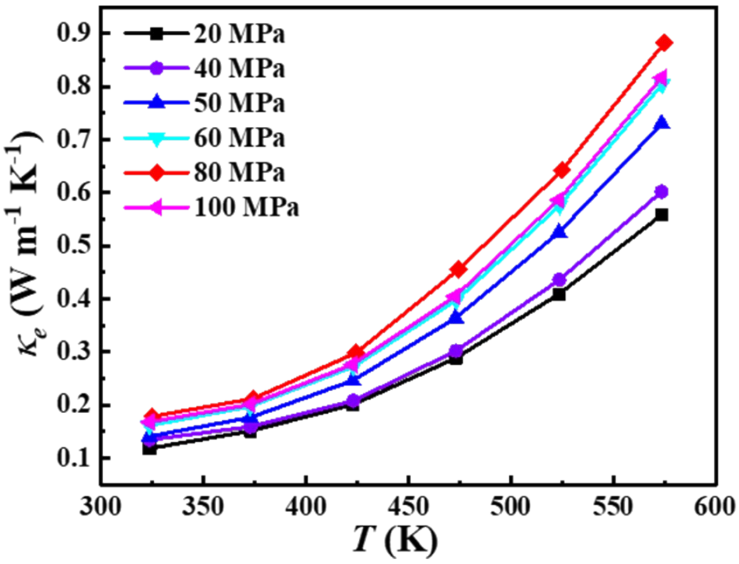

Figure S6. Temperature dependences of carrier thermal conductivity of $MgAg_{0.95}Sb_{0.99}$ samples sintered under the compressive pressure of 20 MPa, 40 MPa, 50 MPa, 60 MPa, 80 MPa and 100 MPa, respectively.

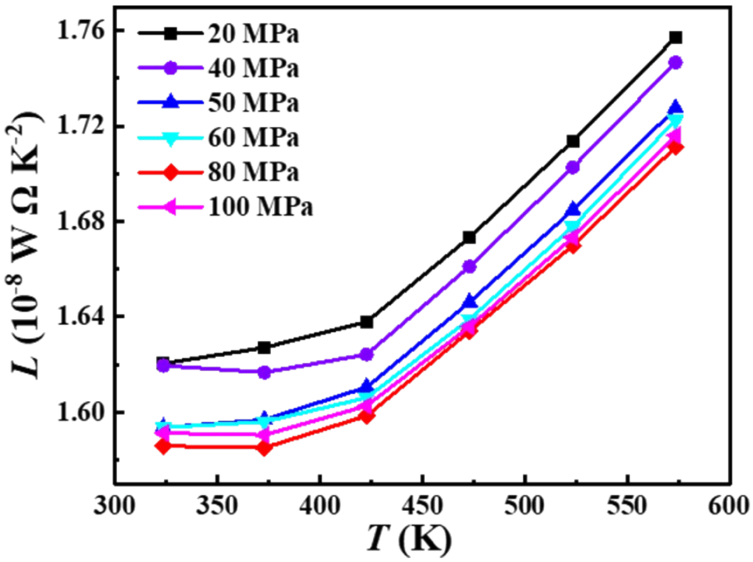

Figure S7. Temperature-dependent Lorentz number of $MgAg_{0.95}Sb_{0.99}$ samples sintered under the compressive pressure for 20 MPa, 40 MPa, 50 MPa, 60 MPa, 80 MPa and 100 MPa, respectively.

Table S1

The full width half maximum (FWHM) and grain size of $MgAg_{0.95}Sb_{0.99}$ samples sintered under the compressive pressure for 20 MPa, 40 MPa, 50 MPa, 60 MPa, 80 MPa and 100 MPa, respectively.

Samples	sintering pressure (MPa)	Crystallographic planes	FWHM (deg.)	Grain size (nm)
$MgAg_{0.95}Sb_{0.99}$	20	(022)	0.160	51.19
$MgAg_{0.95}Sb_{0.99}$	40	(022)	0.151	53.18
$MgAg_{0.95}Sb_{0.99}$	50	(022)	0.135	59.48
$MgAg_{0.95}Sb_{0.99}$	60	(022)	0.128	62.74
$MgAg_{0.95}Sb_{0.99}$	80	(022)	0.124	64.76
$MgAg_{0.95}Sb_{0.99}$	100	(022)	0.132	60.84

Table S2

The density, relative density and porosity of $MgAg_{0.95}Sb_{0.99}$ samples sintered under the compressive pressure for 20 MPa, 40 MPa, 50 MPa, 60 MPa, 80 MPa and 100 MPa, respectively.

Samples	Sintering pressure (MPa)	Density (g cm^{-3})	Relative density (%)	Porosity
$MgAg_{0.95}Sb_{0.99}$	20	5.427	86.01	13.99
$MgAg_{0.95}Sb_{0.99}$	40	5.721	90.67	9.33
$MgAg_{0.95}Sb_{0.99}$	50	5.903	93.55	6.45

$MgAg_{0.95}Sb_{0.99}$	60	6.005	95.11	4.89
$MgAg_{0.95}Sb_{0.99}$	80	6.055	95.95	4.05
$MgAg_{0.95}Sb_{0.99}$	100	6.109	96.81	3.19

The Lorenz number *L* calculation

In this work, the scattering parameter r is assumed to be − 0.5 and the Lorenz number L is deducted from the measured Seebeck coefficient α based on the single parabolic band model using the following equations[1,2]:

$$\alpha = \pm \frac{k_B}{e}\left(\frac{(r+5/2)F_{r+3/2}(\xi)}{(r+3/2)F_{r+1/2}(\xi)} - \xi\right) \quad (1)$$

$$L = \left(\frac{k_B}{e}\right)^2\left(\frac{(r+7/2)F_{r+5/2}(\xi)}{(r+3/2)F_{r+1/2}(\xi)} - \left[\frac{(r+5/2)F_{r+3/2}(\xi)}{(r+3/2)F_{r+1/2}(\xi)}\right]^2\right) \quad (2)$$

$$F_n(\xi) = \int_0^\infty \frac{x^n}{1+e^{x-\xi}}dx \quad (3)$$

$$\xi = \frac{E_F}{k_B T} \quad (4)$$

where E_F is the Fermi energy, ξ is the reduced Fermi energy, k_B is the Boltzmann constant, e is the electron charge, and $F_n(\xi)$ is the Fermi integration. The obtained L is plotted in Figure S7.

References

1. L. Zhao, S. Lo, J. He, H. Li, K. Biswas, J. Androulakis, C. I. Wu, T. P. Hogan, D. Chung, V. P. Dravid, M. G. Kanatzidis, High performance thermoelectrics from earth-abundant materials: enhanced figure of merit in PbS by second phase nanostructures, *J. Am. Chem. Soc*., **2011,** 133, 20476-87.
2. Z. Liu, J. Shuai, J. Mao, Y. Wang, Z. Wang, W. Cai, J. Sui and Z. Ren, Effects of antimony content in $MgAg_{0.97}Sb_x$ on output power and energy conversion efficiency, *Acta Mater.*, **2016,** 102, 17-23.